

INVESTIGATION OF CLEAVAGE FRACTURE UNDER DYNAMIC LOADING CONDITIONS: PART II NUMERICAL ANALYSIS

Johannes Tlatlik

Fraunhofer Institute for Mechanics of Materials IWM, Wöhlerstr. 11, 79108 Freiburg, Germany

johannes.tlatlik@iwmm.fraunhofer.de

Abstract

Part I of this study was an extensive fractographic investigation that covered the topics local crack arrest, and cleavage fracture-inducing mechanisms under dynamic loading situations. Also, it produced data regarding the origin of cleavage fracture. Now, this data is used for the numerical part of this study. First, the development of temperature and strain rate increase at the origin of cleavage fracture is conducted, and linked to discrepancies regarding experiments and the Master Curve concept in a phenomenological way. Then, cleavage fracture controlling mechanical field variables at the origin of fracture are analyzed, whereas very similar conditions regarding crack initiation and propagation are found when compared to quasi-static data. The influence of wave phenomena is examined as well. Finally, micromechanical simulations showed that a local temperature increase at the particle-matrix interface does not influence fracture behavior either, and that conclusively, the actual physical mechanism of cleavage fracture initiation (crack initiation and instability) takes place under the same conditions at elevated loading rates as under quasi-static conditions. Ultimately, the mechanisms responsible for the shortcomings of the Master Curve concept under dynamic loading conditions are identified, and current local approach concepts need to be adjusted to consider local crack arrest to be reliable.

Key Words

Dynamic Fracture Mechanics, Cleavage Fracture, Local Approach, Master Curve Concept, Finite-Element Method

Nomenclature

a	short semi axis of ellipse
b	long semi axis of ellipse
a_0	initial crack length
d_{eq}	diameter of a circle of equivalent area
h	local stress triaxiality
K_I	stress intensity factor
K_{Ic}	fracture toughness
K_{Icd}	dynamic fracture toughness (elastic)

K_{IR}	ASME lower boundary curve
K_J	stress intensity factor (small scale yielding)
$K_{J,IT}$	size corrected stress intensity factor (small scale yielding)
K_{Jcd}	dynamic fracture toughness
$K_{Jcd,IT}$	size corrected dynamic fracture toughness
$K_{Jcd,IT,50\%}$	median fracture toughness curve with 50 % failure probability
x_{cl}	distance of origin of fracture from crack tip
R_m	Tensile Strength
W	specimen height
ε_e^{pl}	accumulated plastic equivalent strain
ε_{matrix}	matrix strain
$d\varepsilon/dt$	strain rate
μ	friction coefficient
σ_I	maximum principal stress
$\sigma_{I,matrix}$	maximum principal stress of matrix
σ_p	particle stress
ASME	American Society of Mechanical Engineers
CMOD	crack mouth opening displacement
FEM	Finite-Element Method
MC	Master Curve
SE(B)	single edge-notched (bending)

1 Introduction

In part I of this study a total of six additional mechanisms was introduced that could potentially impact cleavage fracture behavior under dynamic loading conditions. The mechanisms are

1. temperature increase,
2. strain rate increase,
3. wave phenomena/inertia,
4. local crack arrest,
5. different fracture-inducing mechanisms (i.e. different particle types),
6. local temperature increase at the particle-matrix interface.

Part I consisted of a thorough fractographic examination, and investigating mechanisms 4 and 5. Also, the exact origin of cleavage fracture was documented which is used for this part of this study. Part I proved the strong relevance of local crack arrest for dynamic loading conditions. A general correlation of the probability for crack arrest with fracture toughness was witnessed for all examined crack tip loading rates from 10^3 to 10^5 MPa $\sqrt{m/s}$. Important in this context is the fact that also the very low crack tip loading rates appear to trigger this mechanism as well, which matches the presented discrepancies between Master Curve (MC) and dynamic fracture mechanics experiments (Reichert [1], Mayer [2], Böhme [3], Schindler [4]). This also proves that current local approach concepts do not have the physical fundament to guarantee reliable assessment in terms of cleavage fracture at elevated loading rates. In addition, different primary cleavage fracture inducing mechanisms, such as detachment of MnS, were proven to be

non-existent. Carbide fracture at grain boundaries was identified to be prevailing, which is identical with observations made under quasi-static test conditions.

This part II involves a subsequent numerical investigation to analyze mechanisms 1, 2, 3 and 6. First, the local change in temperature and strain rate at the fractographically obtained origins of cleavage is calculated numerically to discuss the relevance and impact of mechanism 1 and 2 regarding cleavage fracture. Since temperature and strain rate control toughness on a phenomenological level, an analysis of these mechanisms is important for the understanding dynamic fracture in a phenomenological sense. Furthermore, a thorough study of the cleavage fracture controlling mechanical field variables at the origin of fracture is conducted and compared to results from quasi-static investigations, whereas an influence of mechanism 3 is also studied at this level as well. The mechanical field variables inherently conceive the changes in temperature and strain rate, and are the variables which are used for local approach assessment. Finally, a micromechanical approach – involving particle simulations – is applied to examine mechanism 6. Also, the resulting particle stresses upon load are examined too, and compared to similar investigations conducted for quasi-static conditions.

2 Numerical Simulations

2.1 Model and Material Properties

The 3D Finite-Element Method (FEM) model of the SE(B)40-20 specimen used for numerical analysis is displayed in Figure 1, whereas the specimen's symmetries were used according to the image as well. For reasons of numerical stability a crack front with a radius of 5 μm was used with the aid of fully-integrated 8-node volume elements with a linear displacement function. A mean initial crack length a_0 was determined from fractographic examinations. Displacement-controlled load of the striker was applied according to average experimental CMOD-time courses of the respective loading rates, due to the fact that in practice loading rate is not precisely constant over time (this will be discussed in detail later). Anvil and striker were modelled as rigid-body cylinders, respecting compliances and assumed nearly friction-free ($\mu = 0.001$). All calculations were conducted geometrically non-linear with consideration of large plastic deformations by using the ABAQUS implicit solver allowing heat generation and conduction. Temperature-dependent values for standard ferritic steel regarding thermal conductivity, heat capacity, thermal expansion, and density were incorporated, and are displayed in the appendix in Figure 19. Elastic material properties were described by Hooke's law with a temperature-dependent Young's modulus, and the plastic behavior by the v. Mises flow model with isotropic hardening. Strain rate behavior is accounted for by the tabular implementation of the stress-strain curves. Basic data regarding elastic-plastic material properties were obtained from high-speed tensile tests performed by MPA University of Stuttgart (Mayer [5]) at nominal strain rates of 0.004, 0.02, 0.2, 2, 20, and 200 s^{-1} at -20, 0 and 20 $^{\circ}\text{C}$, respectively. Also, additional tests were conducted at 125 $^{\circ}\text{C}$ to obtain reliable data regarding high-temperature behavior. In addition data points for strain rates of 0.02 and 2000 s^{-1} were inter-/extrapolated for all temperatures in order to avoid inter-/extrapolation errors during the calculations. Finally, ductile crack growth was considered as well, in the sense that elements at the crack tip were deleted during the simulations according to the experimentally measured ductile crack lengths as a function of J -Integral. The J -Integral at the crack tip was calculated by ABAQUS contour integrals and weighted according to the respective element size along the crack tip, after which an effective J -Integral was obtained that

represents the entire crack front, and used to calculate the relevant load K_J , and then the size-corrected value of $K_{J,IT}$ according to the terms stated in ASTM E1921 [6].

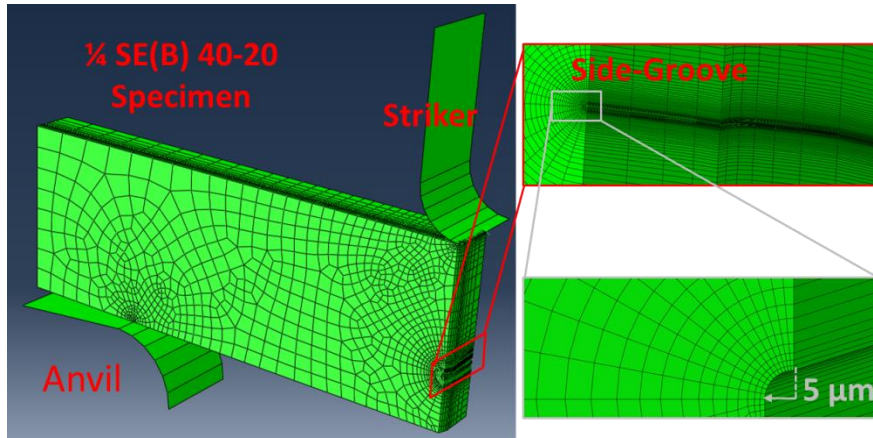


Figure 1: Numerical model used for simulations.

As is the standard procedure, the flow curves from [5] were initially constructed with the assumption of constant temperature and strain rate during the high-speed tensile tests. However, local temperature and strain rate can change heavily during these tests in the area of localization after uniform elongation. Upon consideration of these two mechanisms while re-simulating these high-speed tensile tests, these initial flow curves lead to strong discrepancies between experimental and numerical force-displacement curves (see Figure 2). The numerical results (see Figure 4 for dimensions of the round bar specimen) can be either too stiff, or too soft, depending on the current nominal strain rate. This phenomenon can be explained by taking a closer numerical look at the local strain rate and temperature in the area of localization. Figure 3 displays the development of these two parameters for different nominal strain rates in the area of localization. It is apparent that the local strain rate $d\varepsilon/dt$ increases heavily after uniform elongation or tensile strength by a factor of 10 to 50, which corresponds to higher material strength. This increase is similar for all examined nominal strain rates. On the other hand, temperature increase becomes stronger with increasing nominal strain rate, which corresponds to *lower* material strength. The increased relevance of temperature increase for higher nominal strain rates explains the drop in numerical force-displacement curves in Figure 2. Very low nominal strain rates of 0.004 s^{-1} on the other hand produce too stiff calculations due to the dominance of local strain rate increase. Conclusively, the flow curves need to be adjusted in order to produce reliable stresses, strains, or temperatures in the crack tip region, and are part of this study. The adjustment is performed manually in an iterative process until numerical and experimental force-displacement curves match. The engineering stress-strain curves resulting from the final result for nominal strain rates at $+20 \text{ °C}$ can be observed in Figure 2 right **Fehler! Verweisquelle konnte nicht gefunden werden.** Furthermore, the reliability of this material data set was validated in Reichert et al. [1], in which a high-speed infrared camera was used to measure the temperature in the crack tip region during a dynamic fracture mechanics experiment. Numerical simulations of the experiments implemented with these adjusted flow curves were in excellent agreement with the measured data.

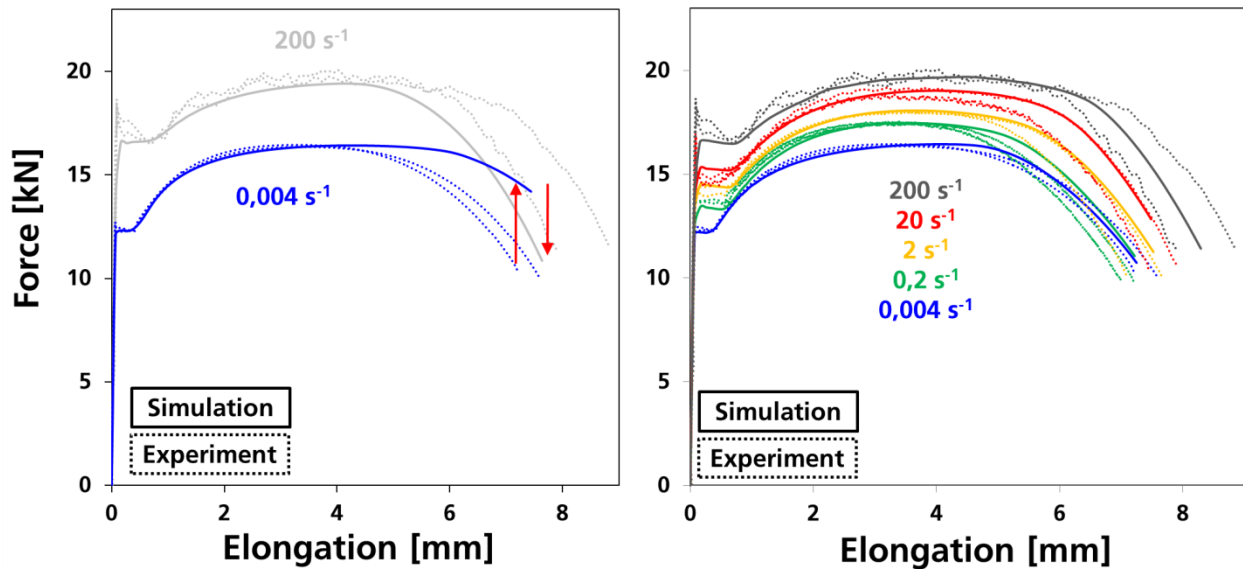


Figure 2: Experimental and numerical force-displacement curves for different nominal strain rates at +20 °C with the original dataset of material properties (left), and the manually adjusted material properties.

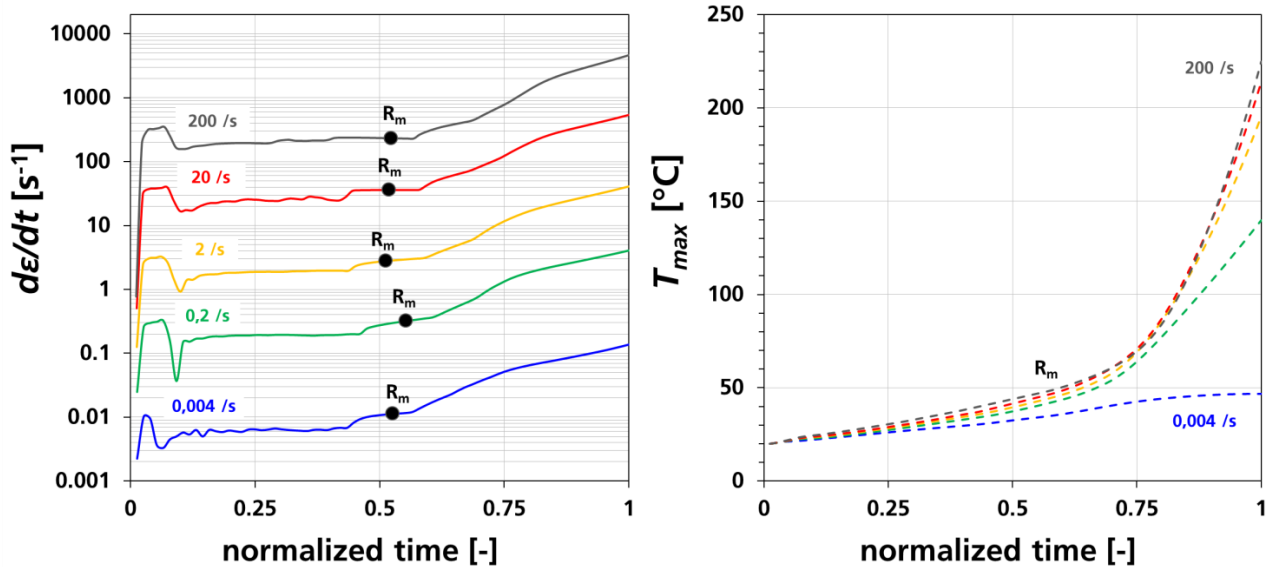


Figure 3: Local strain rate $d\epsilon/dt$ (solid lines) and maximum temperature T_{max} (dashed lines) in the area of localization of a tensile test specimen as a function of normalized time for different nominal strain rates.

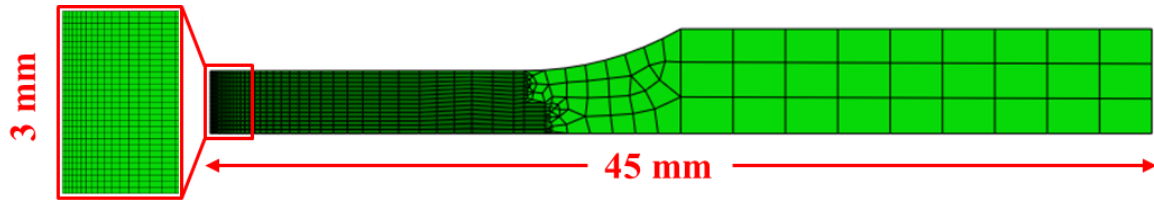


Figure 4: Dimensions of the used rotationally symmetrical round bar specimen.

2.2 Modelling of the Experimental Boundary Conditions

The crack tip loading rates 10^3 , 10^4 , and 10^5 MPa $\sqrt{m/s}$ regarding this experimental database and specimen type correspond to a nominal striker velocity of approximately 0.025, 0.25, and 2.5 m/s, respectively. However, dynamic experiments often show non-constant nominal striker velocity, which can depend on machine type, specimen resistance, or the magnitude of velocity in general. This was also the case for this experimental database, and an example is presented in Figure 5 Left. This instance strongly effects ultimate test time, and therefore time-dependent mechanisms like heat conduction, so the real test conditions need to be considered as accurately as possible in the numerical simulations. In particular, not the real striker velocity is favorable to adjust to, but the actual crack tip opening displacement CMOD of the specimen, in order to correctly represent the time-dependent conditions in the crack tip region. Therefore, the numerical striker velocity was adjusted in an iterative process, so that numerical and experimental CMOD-time developments match. The result can be seen in Figure 6 for the crack tip loading rates 10^4 and 10^5 MPa $\sqrt{m/s}$. Generally, the calculated global forces (at striker) appear slightly lower than experimentally measured, but the CMOD-time developments are in very good agreement, which is essential. Also, inertia or wave effects start to become relevant above 10^5 MPa $\sqrt{m/s}$. Figure 6 shows that this crack tip loading rate produces strong oscillations of the global force curve (solid line), suggesting a strong influence. However, local force measurement by strain gauge reveals only slight oscillations at the crack tip (black dashed line). This was also simulated considering dynamic effects (blue), and a very good reproduction of both global and local force could be achieved. Nevertheless, the conventional simulation without dynamic effects (green) produces very similar global and local force-time developments as well, so that the inertia or wave effects can be neglected on a macroscopic level up to a crack tip loading rate of 10^5 MPa $\sqrt{m/s}$. In addition, the effects do not have a noticeable impact in CMOD either. Ultimately, the calculated development of the crack tip load is in very good agreement with the obtained experimental dynamic fracture toughness values from ASTM E1921 [6], Figure 5 Right.

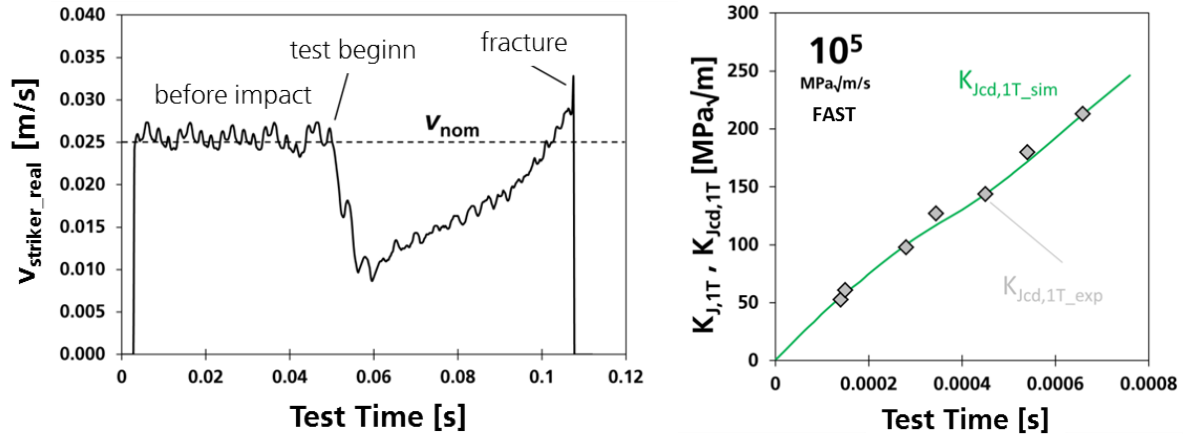


Figure 5: Left: Development of the real striker velocity $v_{striker_real}$ during a fracture mechanics test compared to the nominal striker velocity v_{nom} ; Right: Comparison of numerical crack tip load (green) with the experimental dynamic fracture toughness values from ASTM E1921 (diamonds).

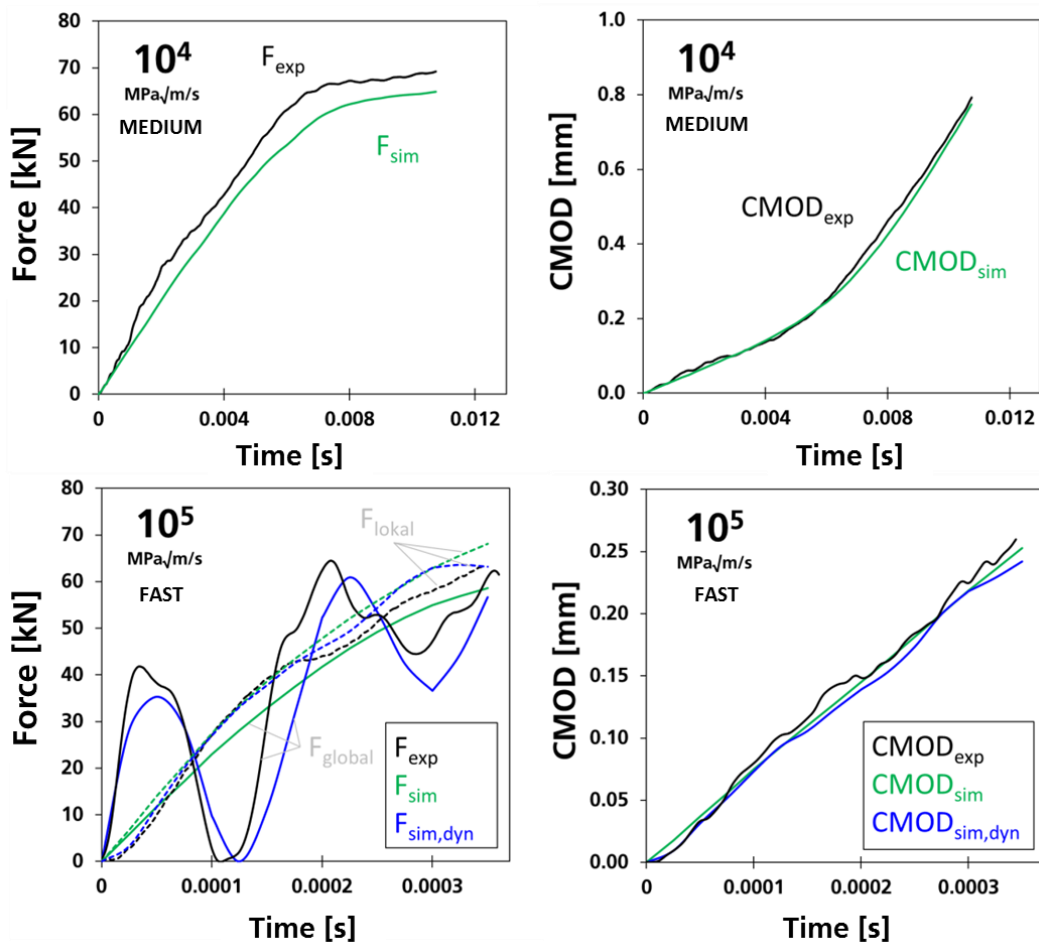


Figure 6: Experimental and numerical global force and CMOD developing over test time. The fast crack tip loading rate was also simulated under dynamic conditions, whereas a local force measurement was conducted here as well (experimentally and numerically) by strain gauges close to the crack tip.

2.3 Analysis of Temperature and Strain Rate Increase at the Origin of Fracture

The temperature dependency of toughness regarding ferritic steels is sufficiently understood and quantified. At lower temperatures dislocation mobility is inhibited, thus the capacity of plastic deformation, and the possibility to relieve stress concentrations or neutralize cracks as well. Very high temperatures provoke the opposite, due to the fact that yield stress is lowered, and ductile damage is triggered more easily than the cleavage fracture mechanism. Because of the low test times at elevated loading rates, heat conduction is not followed by a dissipation of the energy, causing local temperature increase, and different local toughness. On the other hand, this is always accompanied by an increase in strain rate $d\varepsilon/dt$. This mechanism causes a material's toughness to plummet, because dislocation movement is influenced by the very short test times as well. This is referred to as dynamic embrittlement, and is described by the MC through a shift of the respective curves towards higher temperatures.

This section is dedicated to investigating the development, and impact on cleavage fracture, of both of these mechanisms at elevated loading rates. Due to the fact that cleavage fracture originates locally at a more or less distinct location, only the fractographically obtained origins of fracture are of true relevance, and considered in this study. These were determined in part I.

To understand the influence of temperature increase at the crack tip, Figure 7 shows the development of temperature in the cleavage fracture process zone until about $300 \text{ MPa}\sqrt{\text{m}}$ for a crack tip loading rate of 10^4 and $10^5 \text{ MPa}\sqrt{\text{m/s}}$ starting at $20 \text{ }^\circ\text{C}$. It is obvious that a higher crack tip loading rate results in a sharper temperature gradient and higher temperatures, while more test time allows the generated heat to dissipate at medium crack tip loading rates. The expected region of fracture initiation under quasi-static conditions is depicted here as well, which suggests that the higher temperatures resulting from $10^5 \text{ MPa}\sqrt{\text{m/s}}$ do not influence the cleavage initiation process itself, because cleavage takes place further away from the crack tip anyway. In both cases, however, it is clear that fracture origins are influenced by the additional heating, being more pronounced for $10^4 \text{ MPa}\sqrt{\text{m/s}}$. Most importantly, these images demonstrate that the influence of temperature increase is a highly complex phenomenon that is not trivially characterized by the maximum temperature, but also heat dissipation, and the current level of load applied. Considering local crack arrest, it can also be seen that common crack travel distances before arrest (about 30 to $300 \text{ }\mu\text{m}$) are impacted by this heat generation as well. More precisely, once a crack initiates it travels a certain distance with decreasing temperature, and therefore experiencing poorer conditions for crack arrest. Depending on the level of load and crack tip loading rate, Figure 7 shows that after about $100 \text{ }\mu\text{m}$ travel distance a crack can experience temperature drops of more than $10\text{-}15 \text{ }^\circ\text{C}$. This is in agreement with the observation that very large arrest islands are not seen on the fracture surface. Despite the temperature gradient at the crack tip however, generally better conditions for arrest are produced by the dynamic testing conditions due to the heating mechanism.

Figure 8 shows the calculated development of the temperature at the individual origins of initiation. It can be seen that generally initiation occurs at higher temperatures for higher fracture toughness values. Also, and as expected, temperature increase is more rapid for higher crack tip loading rates. This is also obvious while comparing T_{ini} of different crack tip loading rates at the same load of i.e. $125 \text{ MPa}\sqrt{\text{m}}$ (best visible for a test temperature of $0 \text{ }^\circ\text{C}$). This is due to the fact that the shorter test times retard heat conduction. However, this does not imply that the *final* initiation temperature T_{ini} is higher as well. Lower crack-tip loading rates indeed do allow more heat dissipation which weakens this effect, but they also result in higher fracture toughness values, which in turn cause more plastic deformation, and generate more heat. In

other words, lower crack tip loading rates do not necessarily lead to cleavage initiation at lower temperatures compared to higher loading rates, because cleavage initiation is a very local event, and the location matters. Conclusively, the effect of crack tip heating for dynamic loading situations is not only relevant at high loading rates but also at medium loading rates. This agrees well with the discrepancies between dynamic experiments and MC assessment (Reichert [1], Mayer [2], Böhme [3], Schindler [4]).

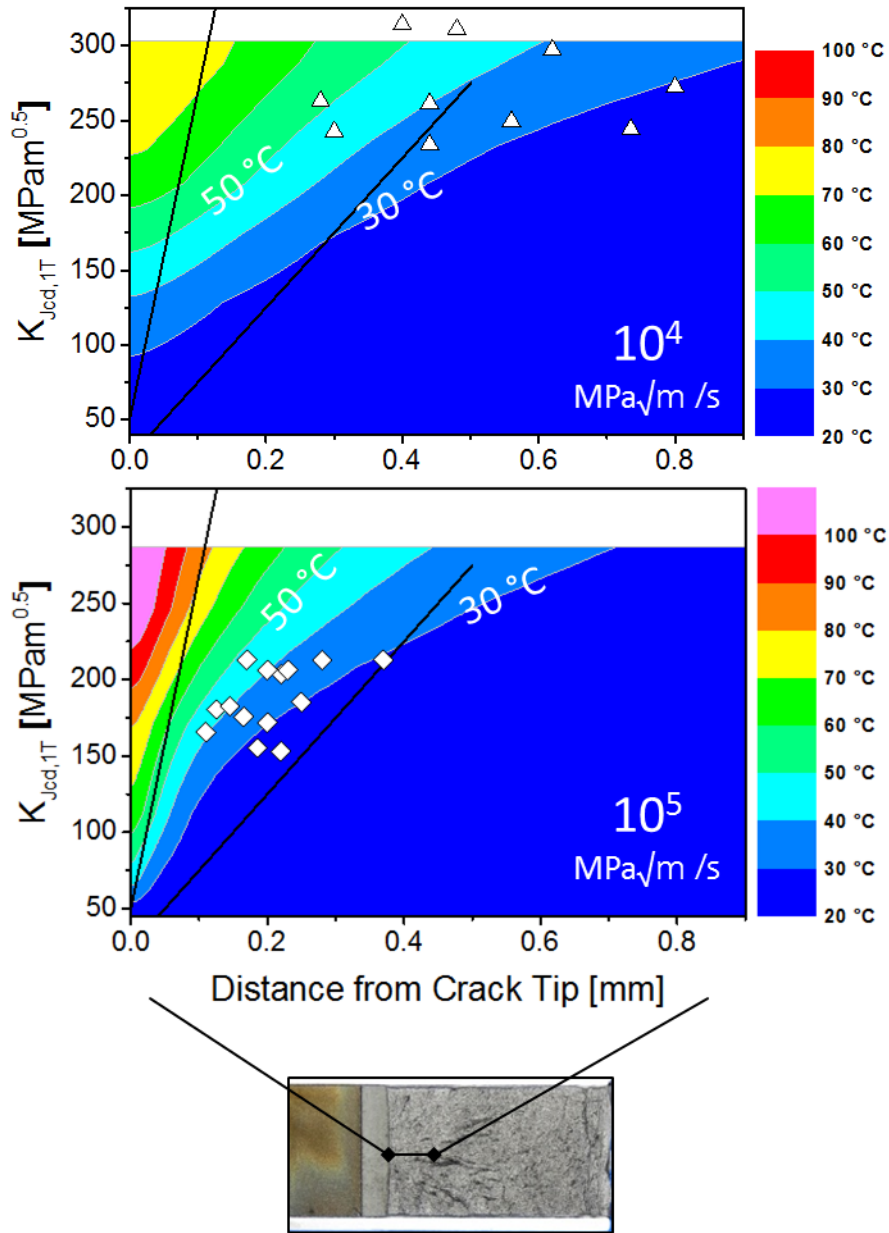


Figure 7: Numerically calculated development of the temperature in the crack tip region at increasing load for two different crack tip loading rates (starting at 20 °C). Shown are also the fractographically determined origins of fracture for the respective test series.

Figure 9 displays the development of the embrittling effect of local (plastic) strain rate increase. In particular, the time-dependent change of the plastic strain at the individual origin of fracture was extracted and calculated from one increment to another, and plotted. The image will be explained by the example of high crack tip loading rates (three series of diamonds). Regardless of test temperature, an increase of crack driving force $K_{J,IT}$ causes a similar increase in local strain rate $d\varepsilon/dt$ at the origin of fracture, yet lower test temperatures lead to earlier failure. The incline in local strain rate $d\varepsilon/dt$ is rather rapid in the beginning, and reaches a level of saturation also independent of the test temperature around a crack driving force $K_{J,IT}$ of $125 \text{ MPa}\sqrt{\text{m}}$. The same progress can be witnessed for all other crack tip loading rates, differing only in the level of saturation. The point (or load) of saturation, however, appears to be rather constant for all conditions at about $K_{J,IT} = 125 \text{ MPa}\sqrt{\text{m}}$. For example series at $-20 \text{ }^\circ\text{C}$ (blue shades) never reach this level, because failure occurs prior to this. So conclusively, the dynamically induced embrittling effect of strain rate increase actually loses relevancy with higher loads, and stagnates around $K_{J,IT} = 125 \text{ MPa}\sqrt{\text{m}}$, whereas temperature increase does not.

A better way to compare the competing mechanisms is shown Figure 10 in which local strain rate is plotted against local temperature. Looking back, the experimental data states that elevated loading rates produce lower fracture toughness values than quasi-static testing conditions at similar temperatures. The dynamic embrittlement is caused by the rapid increase in local strain rate especially for low loads $< K_{J,IT} = 100 \text{ MPa}\sqrt{\text{m}}$. heating temperature increase at the origin of initiation is rather insignificant until this point. Because local strain rate reaches a specific level of saturation, the effect of dynamic embrittlement loses significance, and the role of (adiabatic) temperature increase becomes more prominent (development of graphs to the right). The result is impeded cleavage initiation conditions with higher loads $K_{J,IT}$ that in turn presumably cause higher fracture toughness values than expected. This explanation also matches the progressive character of these experimental discrepancies towards higher fracture toughness values, or in other words, the necessary increasing steepness of the dynamic Master Curve with higher loads. This is the case for all the examined crack tip loading rates.

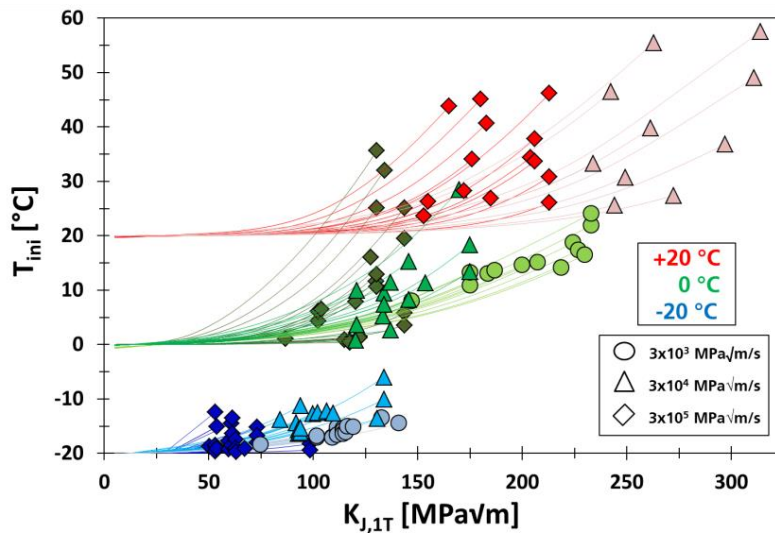


Figure 8: Numerically calculated development of the temperature at the origin of initiation T_{ini} over crack driving force $K_{J,IT}$.

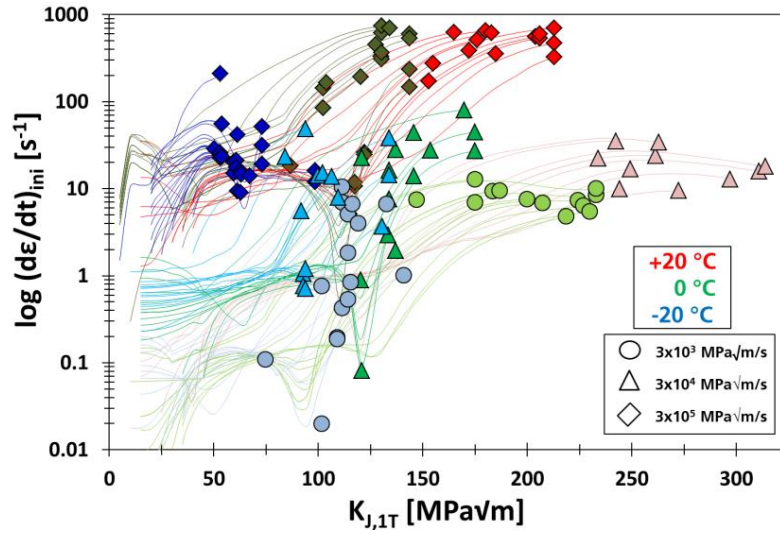


Figure 9: Numerically calculated development of the local strain rate $d\varepsilon/dt$ at the origin of initiation as a function of crack driving force $K_{J,1T}$.

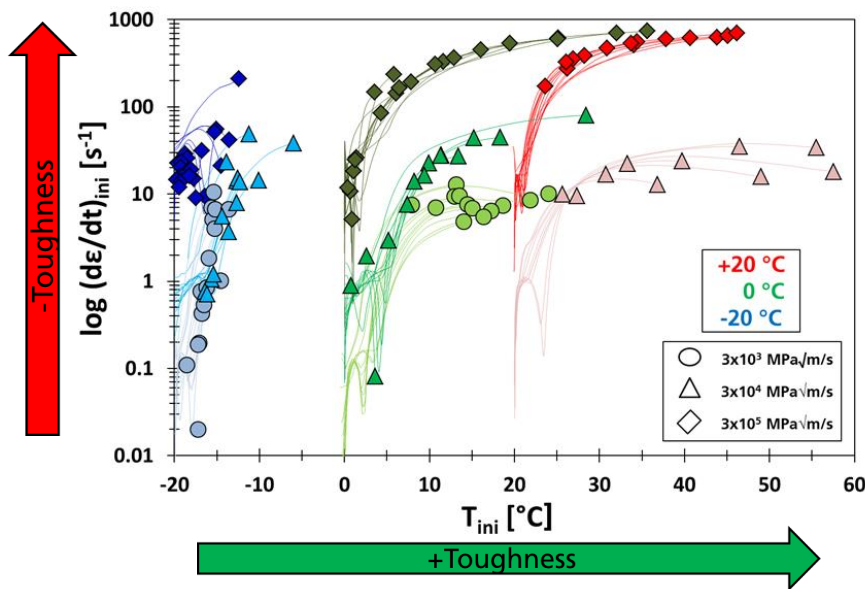


Figure 10: Development of the local strain rate $d\varepsilon/dt$ at the origin of initiation as a function of temperature at the origin of initiation T_{ini} .

2.4 Impact of Inertia and Wave Phenomena

The impact of inertia and wave phenomena has already been briefly discussed on a macroscopic level involving force and crack mouth opening displacement, and identified as non-existing, or considered negligible for the highest crack tip loading rate (Figure 6). This mainly has to do with the ratio of $a_0/W \approx 0.3$ which reduces wave phenomena. The purpose of this section is to analyze the relevance of inertia and wave phenomena on a microscopic level regarding a possible oscillation of the mechanical field variables. Figure 11 shows the development of maximum principal stress σ_I , and stress triaxiality h

over test time at a distance of 130 μm from the crack front for a simulation with and without the consideration of dynamic effects for a high crack tip loading rate of $10^5 \text{ MPa}\sqrt{\text{m/s}}$. Stress triaxiality h remains almost completely unaffected, while σ_I experiences a moderate deviation at the beginning, and very slight oscillations around the quasi-statically calculated value towards the end of the experiment. The deviation at the beginning is irrelevant in terms of cleavage fracture initiation, because really only the conditions at failure are of interest. Since this mechanism also only becomes noticeable for the highest crack tip loading rate of $10^5 \text{ MPa}\sqrt{\text{m/s}}$, and the ramifications appear only very marginal, negligence is justifiable, and all following simulations can be carried out in that manner. It is very likely, however, that these oscillations become more profound for higher crack tip loading rates of $10^6 \text{ MPa}\sqrt{\text{m/s}}$ and more, yet these highly dynamic loading situations are not considered in this work. Also, a higher crack depth ratio $a_0/W > 0.3$ would most likely result in a higher relevance of wave phenomena, as well (Böhme [7]).

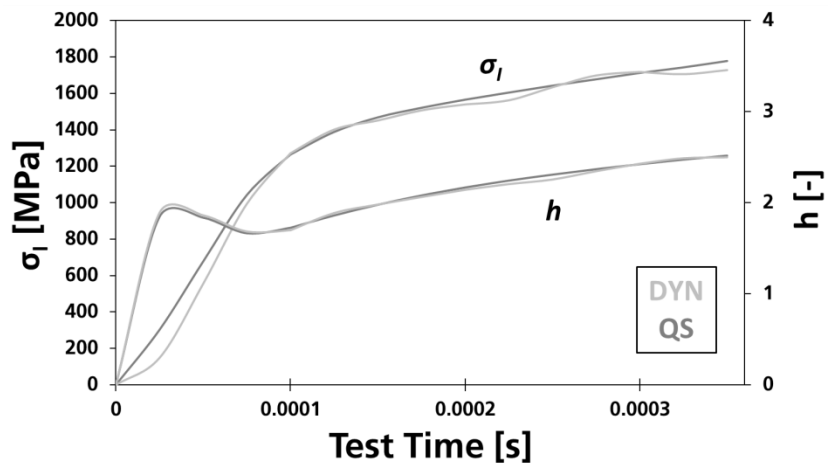


Figure 11: Comparison of maximum principal stress and stress triaxiality at an origin of fracture (distance 130 μm from crack tip) for simulations with (DYN) and without (QS: means without inertia/waves) dynamic effects for a high crack tip loading rate of $3 \cdot 10^5 \text{ MPa}\sqrt{\text{m/s}}$.

2.5 Analysis of Cleavage Fracture Controlling Mechanical Field Variables

The mechanical field variables: accumulated plastic equivalent strain ε_e^{pl} , local stress triaxiality h , and maximum principal stress σ_I govern the probability of brittle failure in local approach concepts. Inherently, these should conceive the additional dynamic mechanisms of temperature and strain rate increase, as well as wave phenomena, because the mechanical field variables change according to these adaptations. Fractographic investigations revealed rather strong differences regarding the origin of fracture (compared to quasi-static data), yet it is not clear if the conditions there are different as well, or if fracture simply takes place in a different location x_{cl} and at a different global load $K_{J,IT}$ with similar conditions that are already known from quasi-static examinations. This section is dedicated towards analyzing these conditions (defined by the mechanical field variables) at the moment and location of fracture under dynamic loading conditions in comparison to quasi-static investigations by Hohe et al. [8].

The investigations by Hohe et al. [8] are the basis of a local approach model which treats defect nucleation, and defect instability separately. More defects are produced by an increase in strain ε_e^{pl} , while the criticality of the fresh defects is in turn controlled by local stress triaxiality h (sharp or blunted crack). Earlier work by Hohe et al. [9] revealed that the two quantities are not independent of each other, but rather interrelated. Low values of plastic strain ε_e^{pl} correspond to high levels of stress triaxiality, and higher levels of plastic strain ε_e^{pl} correspond to much lower stress triaxialities. Very high levels of plastic strain ε_e^{pl} are needed in the latter scenario to create a possible critical or sharp microdefect, because the low levels of stress triaxiality promote blunting. This relation is used and interpreted as a failure curve describing the nucleation of a critical microdefect, and shown in Figure 12 as the dashed line. Quasi-static results are not displayed here, yet in all cases this unique failure curve is approached, but not crossed, and followed in a parallel manner towards higher values of plastic strain. Figure 12, however, shows the calculated results under dynamic loading involved in this present study. It is obvious that the described relation develops very similarly for various crack tip loading rates, and a new failure curve for dynamic conditions would be nearly identical, both in slope and distance, than the one proposed in [8] and shown in Figure 12 under quasi-static conditions. Since this relationship governs the probability of critical microdefect nucleation, it is the conclusion of the author that the general mechanism does not change at elevated loading rates either. This also matches the fractographic results from part I in the sense that the main cleavage fracture triggering mechanism (carbide cracking at grain boundaries) was identified to remain the predominant one at elevated loading rates as well.

Defect instability is controlled by maximum principal stress σ_I in all important local approach models, and a certain minimum level is interpreted as a requirement for brittle failure. Also, according to the Griffith Criteria [10] the necessary value of σ_I for instability varies with defect size. Since the maximum defect or brittle particle size is limited in practice, there must also be a minimum value or threshold beneath which global failure does not occur. Data from Hohe et al. [7] observed σ_I values independent of temperature, fracture toughness or specimen geometry. No σ_I values beneath 1500 MPa were observed, whereas approximately 1900 MPa demonstrates the maximum value. The numerically calculated maximum principal stress σ_I at the origin of fracture for dynamic loading conditions can be seen in Figure 13. It is apparent that identical observations can be made here as for the described quasi-static conditions. Therefore, it is also the author's conclusion that the general mechanism of microdefect instability is also not changed by the dynamic loading conditions.

Ultimately, the analysis of the cleavage fracture controlling mechanical field variables allows the preliminary conclusion that cleavage fracture initiation (defect evolution and instability mechanism) has the identical physical background under dynamic and quasi-static loading conditions. Local approach models by Beremin [11], Faleskog [12], or Hohe [8] should therefore correctly describe the physical mechanism of defect evolution and instability. In other words, cleavage fracture only takes place in a different location and at different global loads compared to quasi-static conditions due to temperature increase at the crack tip in combination with local arrest phenomena. However, the relevance of the local temperature increase at the particle-matrix interface (mechanism 6) is not considered at this point, due to the fact that particles are not included in these macroscopic simulations. The next section will be dedicated to clarifying the relevance of this mechanism.

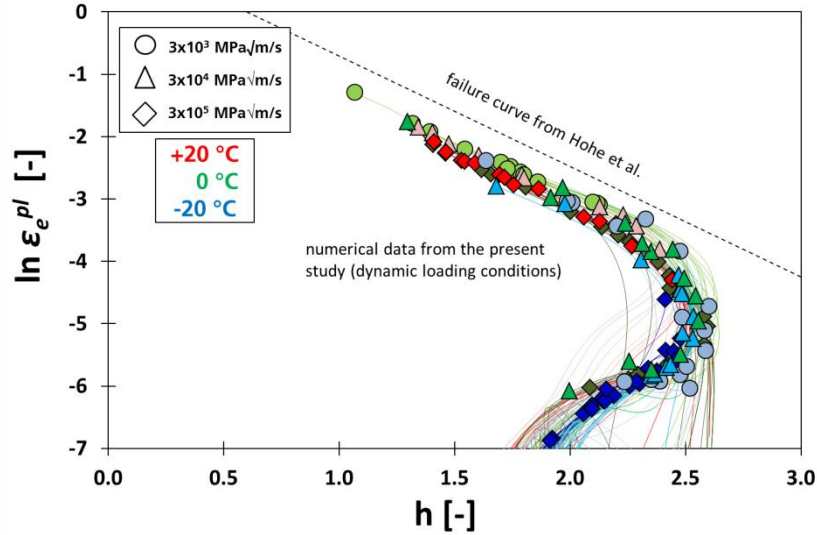


Figure 12: Development of plastic strain over stress triaxiality coefficient during dynamic loading conditions until fracture. Displayed is also the failure curve from Hohe et al. [8].

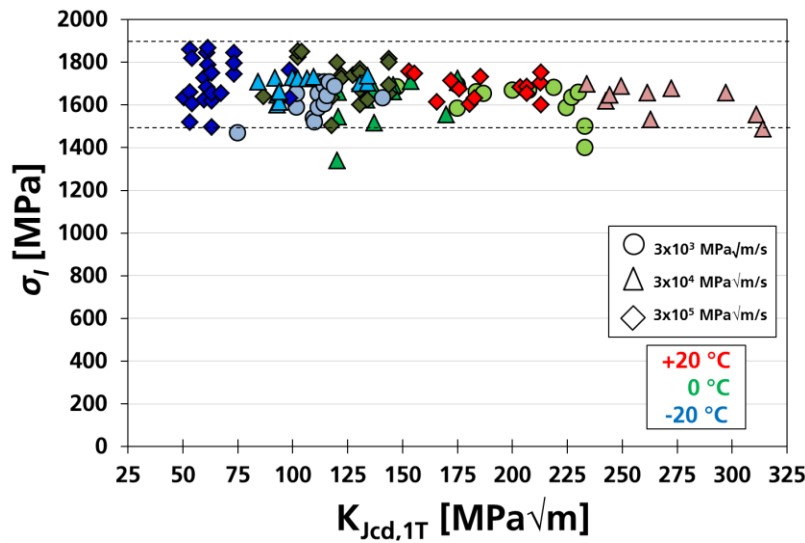


Figure 13: Maximum principal stress at the origin of fracture at failure as a function of fracture toughness. Displayed is also the region or scatter of values (1500 to 1900 MPa) for quasi-static test calculated by Hohe et al. [8].

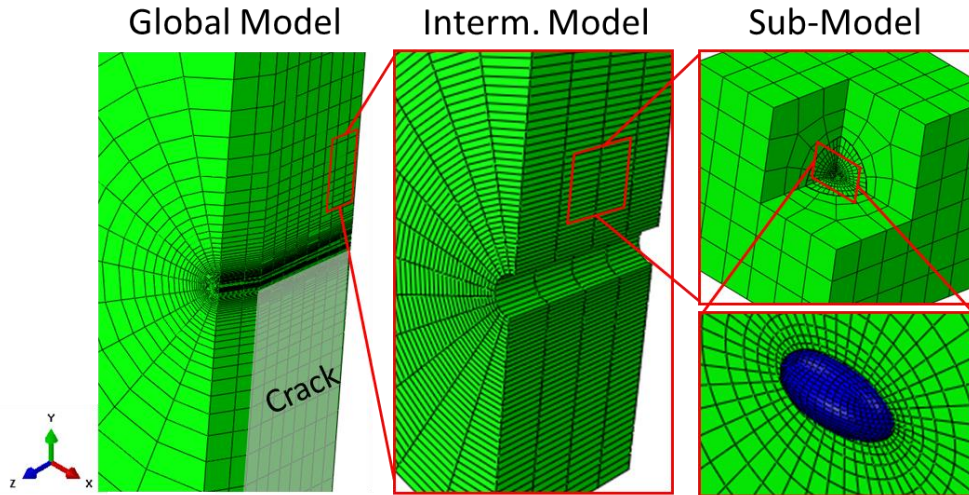
2.6 Micromechanical Simulations

A micromechanical investigation of the microdefect nucleation mechanism is of special interest, because it provides the closest representation of the actual physical mechanism. This section will focus on investigating the relevance of the local temperature increase at the particle-matrix interface (mechanism 6), and also compare the resulting effective load for a particle within the matrix to similar calculations made by Hardenacke [13] for quasi-static conditions.

In advance, microstructure analysis of the material was performed to ascertain particle characteristics (size, shape). The average size of the elliptical particles was identified to be about $d_{eq} \approx 0.16 \mu\text{m}$ (d_{eq} : diameter of a circle of equivalent area), while the average semi axis ratio a/b of the approximated ellipses was characterized as $a/b \approx 0.5$. In order to perform micromechanical simulations, a small sub-model was generated containing a single idealized brittle particle, and loaded with representative load histories. This procedure is illustrated in Figure 14 in which the orientation of the particle can be seen for the first investigations. The brittle particle was modelled with the same temperature-dependent physical properties as the ferritic matrix, yet a slightly higher Young's-Modulus of 237,000 MPa was implemented, accompanied by no plastic material behavior.

In a first step, an intermediate model is extracted from the already presented and calculated global model, and meshed more densely. The boundaries of this intermediate model are subjected to the node-displacements at the respective locations of the global model, and the temperature-development within the intermediate model is mapped from the global model as well. Subsequently, this model is re-calculated, after which the actual sub-model containing a particle is subjected to displacement and temperature analogously with results from the intermediate model (needed in order to prevent interpolation errors due to the rather coarse mesh of the global model). The result is a very fine-meshed model with the exact stress-strain-temperature field from the global simulations. At the end of the simulations the stress-strain-temperature fields of the global and sub-model were manually checked for agreement to prevent errors of the method. The mentioned representative load histories are then created solely by defining the distance of the sub-model from the crack tip x_{cl} , in combination with the crack driving force $K_{J,IT}$. The representative load histories were derived statistically from fractography and experiments, and are not discussed in detail at this point. As one example though, the load history of $x_{cl,50\%}$ (representing the median distance of the origin of fracture from the crack tip for a specific test series), and $K_{Jcd,IT,50\%}$ (representing the median fracture toughness of a specific test series) will be used.

In order to first analyze the relevance of the local temperature increase at the particle-matrix interface, calculations of the sub-model without temperature mapping, but rather with direct calculation need to be performed. This means that heat conduction in the macroscopic crack tip region of the global model is not considered (heat flowing in and out of the sub-model), but in this case only the relevance of the mechanism is examined, and not the actually resulting temperature. Figure 15 shows the calculated plastic strain, and the temperature of the near vicinity of an idealized particle with the ferritic matrix. It can be seen that indeed, local concentrations of plastic strain of up to 50 % occur at the particle-matrix interface upon load. In this particular case a high crack tip loading rate of $10^5 \text{ MPa}\sqrt{\text{m/s}}$ at $-20 \text{ }^\circ\text{C}$ test temperature at $x_{cl} = 100 \mu\text{m}$ and $K_{J,IT} = 100 \text{ MPa}\sqrt{\text{m}}$ are shown, which cause a comparatively high plastic strain of the matrix of about 13 %. Figure 15 also shows that despite the local concentrations of plastic strain practically no local temperature gradient is created. In other words, the generated heat is conducted away from the particle-matrix interface very quickly. This is explained by the very small dimensions of the particle (less than $1 \mu\text{m}$ length), because heat conduction, or the presence of adiabatic conditions, is highly governed by the respective distances. Ultimately, it was demonstrated that even for the highest crack tip loading rate of $10^5 \text{ MPa}\sqrt{\text{m/s}}$, and rather large plastic strains, local temperature increase at the particle-matrix interface is negligible. Therefore, this mechanism does not need to be considered separately in local approach concepts.



Application of Local Load Histories:
 x_{cl} and $K_{Jcd,1T}$

Figure 14: Illustration of the used sub-model technique with global, intermediate, and sub-model.

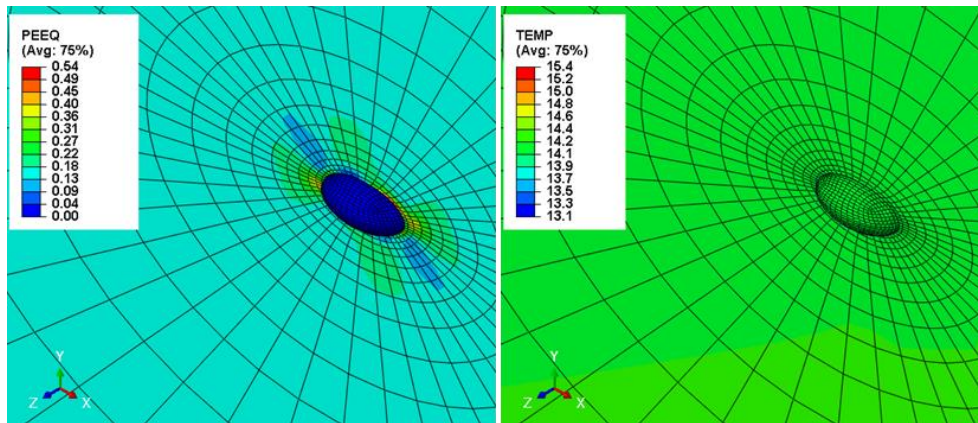


Figure 15: Plastic strain and temperature development of the particle and the near vicinity subjected to 10^5 MPa $\sqrt{m/s}$ at -20 °C test temperature for a given representative local load history.

As already introduced, Hardenacke [13] conducted very similar micromechanical simulations under quasi-static conditions to investigate the resulting load for a particle within the ferric matrix for certain load histories. To further confirm that the actual physical mechanism of cleavage fracture initiation takes place under the same physical conditions at elevated loading rates, equivalent simulations were selectively conducted in this work as well. In particular, the resulting particle stress σ_p (average maximum principal stress weighted according to the respective element size) was analyzed for different particle sizes, shapes (semi axis ratios a/b), and orientations regarding the direction of main loading (x -direction in Figure 14).

Like in Hardenacke [13], the impact of particle size was found to be negligible regarding the resulting particle stress σ_p . However, particle orientation and particle shape have a strong impact on particle stress. As an example, Figure 16 visually shows the relevant particle shapes a/b identified from fractography, and the resulting particle stress for a given dynamic load history of $x_{cl,50\%}$ at the load $K_{Jcd,1T,50\%}$. A smaller aspect ratio, or in other words a more stretched particle, leads to significantly higher particle stresses σ_p , and therefore a higher probability for a microdefect nucleation. Analogously, the impact of particle orientation regarding the direction of main loading (for the average particle shape of $a/b = 0.5$) is presented in Figure 17. The highest particle stress results if the large semi axis of the particle coincides with the main direction of load. Moreover, Figure 18 now shows the interrelated influence of particle shape and orientation on particle stress for different configurations. It is obvious that the impact of one of the two parameters regarding particle stress is highly dependent on the other parameter. That is to say that for example a change in particle shape a/b can have no impact on particle stress if the orientation is high enough. Additionally, Figure 18 shows this relationship for different crack tip loading rates and different matrix conditions (maximum principal stress $\sigma_{I,matrix}$ and strain ϵ_{matrix} of the matrix), which reveal very similar coherences on a qualitative level, and no differences regarding load rate.

All of these discussed results and observations are qualitatively in excellent agreement with analogous studies performed in Hardenacke [13] for quasi-static conditions. Naturally, some minor differences are explained by the different individual local load histories, and also by the different elastic-plastic material properties, which are evident even among the various quasi-static conditions. Yet, this section too additionally confirms the previous results, stating that the physical mechanism of cleavage fracture itself is not changed upon dynamic loading.

Furthermore, the real particles would most likely fracture at much lower matrix deformations than witnessed in this study due to the irregular and not idealized elliptical shape. The formation of local singularities regarding the true irregular shapes would lead to much more favorable crack formation and therefore also failure. Nevertheless, the aim of this study was to compare the resulting conditions for failure compared to the mentioned study under quasi-static conditions.

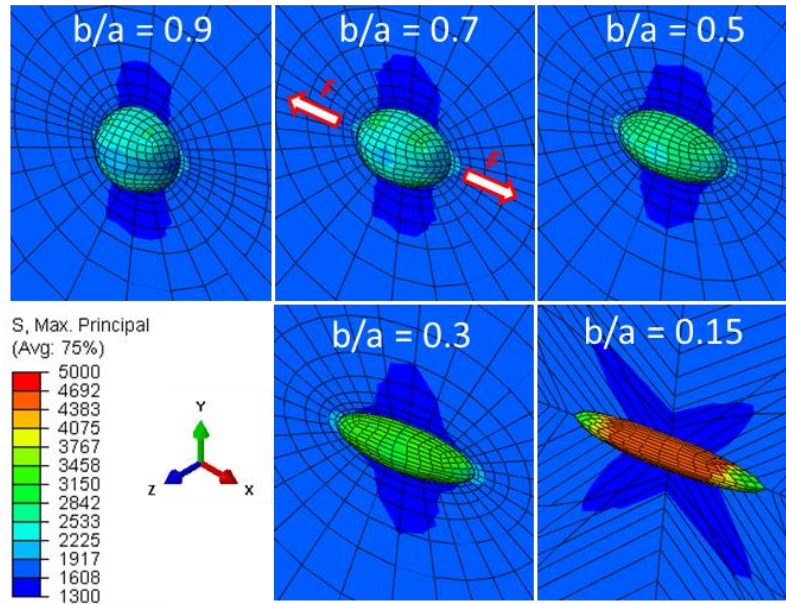


Figure 16: Visualized particle stress for the complete range of the fractographically determined particle shapes a/b at an exemplary origin $x_{cl,50\%}$ and exemplary load $K_{Jcd,1T,50\%}$ at a crack tip loading rate of $10^3 \text{ MPa}\sqrt{\text{m/s}}$.

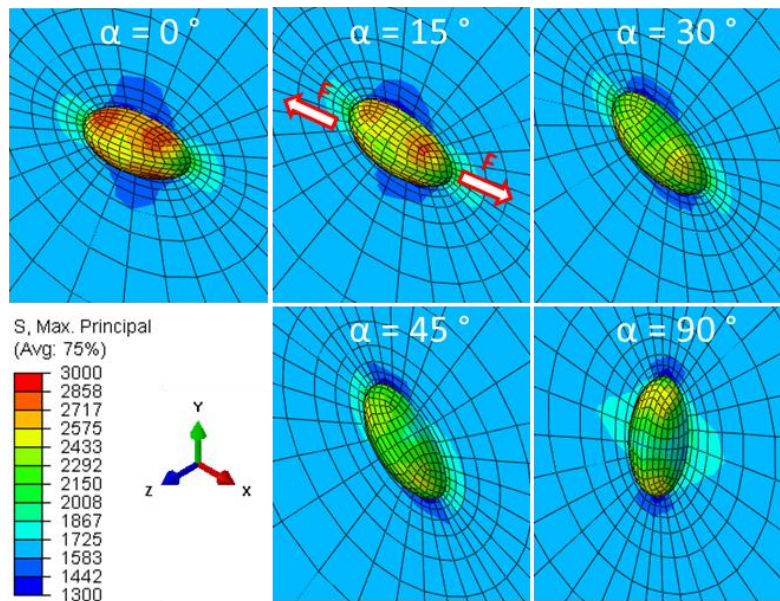


Figure 17: Visualized particle stress for the complete range of possible particle orientations at an exemplary origin $x_{cl,50\%}$ and exemplary load $K_{Jcd,1T,50\%}$ at a crack tip loading rate of $10^3 \text{ MPa}\sqrt{\text{m/s}}$.

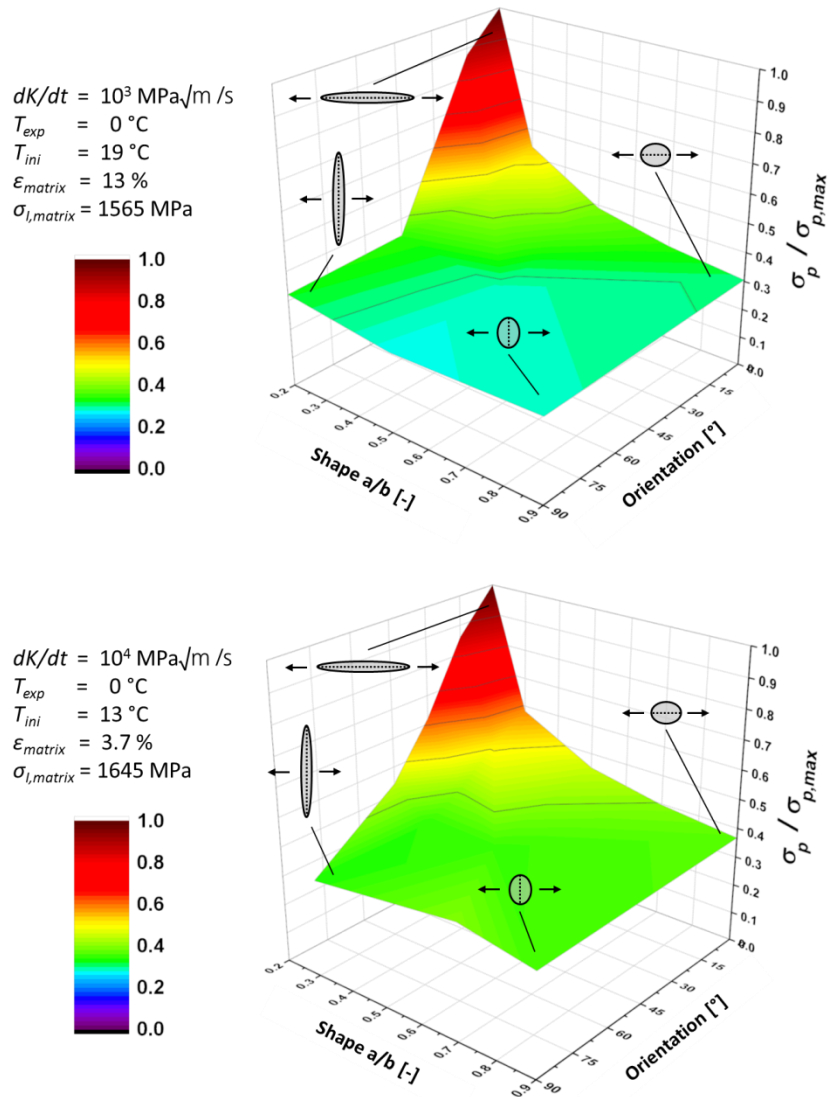


Figure 18: Overview of the interrelated influence of particle shape and orientation on the resulting particle stress for two different crack tip loading rates and different matrix conditions.

3 Conclusions

Cleavage fracture under dynamic loading conditions was investigated numerically (and fractographically in part I) on a phenomenological level (increase in temperature and strain rate), on the level of the cleavage fracture controlling mechanical field variables (accumulated plastic equivalent strain ϵ_e^{pl} , local stress triaxiality h , and maximum principal stress σ_I), and a micromechanical level (resulting particle stress σ_p). The following conclusions can be made from part II of this study:

- Initially, local strain rate at the origin of fracture increases rapidly, and continuously *decreases* material toughness until about $K_{J,IT} = 100 - 125 \text{ MPa}\sqrt{\text{m}}$, after which a crack tip loading rate specific, but always stagnating, strain rate is reached.

- Local temperature at the origin of fracture only gradually increases at low $K_{J,IT}$ –values, yet a linear and constant progression is observed later that depends on crack tip loading rate, continuously *increasing* material toughness at higher $K_{J,IT}$ –values.
- Local temperature increase close to the crack tip very likely favors local arrest events.
- The terms for cleavage fracture initiation (crack evolution and instability) are therefore impeded at higher $K_{J,IT}$ –values, which corresponds to the observed discrepancies between Master Curve and experiments.
- This leads to higher experimental fracture toughness values, yet the mechanical field variables at the origin and load of fracture are identical to observations made for quasi-static conditions.
- In addition to this, micromechanical simulations regarding particle stresses confirmed the fact that the physical mechanism of cleavage fracture itself is identical at elevated loading rates, and it only takes place in different locations and also different macroscopic loads.
- Wave phenomena/inertia can be neglected for crack tip loading rates $\leq 10^5$ MPa $\sqrt{m/s}$.
- The additional temperature increase at the particle-matrix interface can be neglected as well.

The fractographic evidence from Part I of this study agrees with the fact that the physical mechanism of crack evolution and instability takes place under the same conditions, because the same primary fracture-inducing mechanism (carbide cracking at grain boundaries) was identified for dynamic and quasi-static testing conditions. In terms of current cleavage fracture assessment methods the following conclusions can be made from both parts of the study:

- The shortcomings of the Master Curve regarding elevated loading rates are now explained by the increase of strain rate, temperature, and the probability for local crack arrest. The attempts to adjust the Master Curve at elevated loading rates are now justified by these mechanisms.
- Local approach concepts have the physical background to correctly describe cleavage fracture behavior in terms of defect evolution and instability (if suitable temperature- and strain rate-dependent flow curves are provided), yet global fracture is heavily influenced by local crack arrest as well (postponement of failure). Therefore, these local concepts (based on the weakest link concept by Mudry [15]) need to be adjusted or extended. This will be subject of further investigations.

Due to crack arrest the experimental data (Böhme et al. [14]) is not well described by Weibull distribution. A more elegant way to adjust the MC could be to adjust the parameter K_{min} instead of the shape parameter, since it can be justified physically by crack arrest, and it should be temperature-dependent. This, however, would make it also dependent on crack tip loading rate, and therefore very unfavorable due to the primarily practical and also non-physical background of the MC concept.

Acknowledgement

The investigations were supported by the German Federal Ministry for Economic Affairs and Energy under the support code 1501495 which is thankfully acknowledged by the authors.

4 Appendix

Parameter	Sign	Value	Temperature [°C]	Unit
stiffness	E	221235	-175	MPa
		220500	-150	MPa
		205500	100	MPa
		199500	200	MPa
		190000	500	MPa
Poisson's Ratio	ν	0	all	-
thermal	α	0	-200	/°C
Expansion		0	92	/°C
(reference: 25 °C)		0	300	/°C
heat conduction	λ	46.5	-20	mJ/(s mm °C)
		45.0	20	mJ/(s mm °C)
		42.4	92	mJ/(s mm °C)
		38.3	178	mJ/(s mm °C)
		36.7	293	mJ/(s mm °C)
		35.6	384	mJ/(s mm °C)
		33.4	490	mJ/(s mm °C)
specific heat capacity	C	4.150E+08	-20	mJ/(ton °C)
		4.350E+08	20	mJ/(ton °C)
		4.700E+08	92	mJ/(ton °C)
		5.100E+08	178	mJ/(ton °C)
		5.500E+08	293	mJ/(ton °C)
		5.800E+08	384	mJ/(ton °C)
		6.400E+08	490	mJ/(ton °C)
density	ρ	7.840E-09	-20	ton/mm ³
		7.825E-09	20	ton/mm ³
		7.800E-09	92	ton/mm ³
		7.770E-09	178	ton/mm ³
		7.740E-09	293	ton/mm ³
		7.710E-09	384	ton/mm ³
		7.670E-09	490	ton/mm ³
inelastic heat fraction	-	0.9	all	-

Figure 19: Overview of the used temperature-dependent physical properties.

References

- [1] Reichert, T., Böhme, W. and Tlatlik, J.: Modified Shape of Dynamic Master Curves due to Adiabatic Effects, 21st European Conference on Fracture, ECF21, 20-24 June 2016, Catania, Italy, 2016.
- [2] Mayer, U., Reichert, T., Tlatlik, J.: Fracture Mechanics at Elevated Loading Rates in the Ductile to Brittle Transition Region, 2017 ASME Pressure Vessels & Piping Conference, 16-20 2017, Waikoloa, Hawaii, USA, 2017.
- [3] Böhme, W., Reichert, T., Mayer, U.: Assessment of dynamic fracture toughness values KJc and reference temperatures $T_{0,x}$ determined for a German RPV steel at elevated loading rates according to ASTM E1921, SMiRT-22, San Francisco, California, USA, August 18-23, 2013, Division II, Fracture Mech. and Struct. Integrity, 2013.
- [4] Schindler, H. J. and Kalkhof, D.: Lower bounds and saturation effects of dynamic fracture toughness in the brittle-to ductile transition regime of ferritic steels, to be published at 22nd Int. Conf. on Structural Mechanics in Reactor Technology, SMiRT-22, San Francisco, USA, 2013.
- [5] Mayer, U., MPA-provisional result of the collaborative project: Analysis and Validation of Fracture Mechanical Assessment Methods under Dynamic Loading, personal message, June 2015.
- [6] ASTM Standard E 1921-16: Standard test method for determination of reference temperature T_0 for ferritic steels in the transition range, ASTM International, West Conshohocken, PA, 2016.
- [7] Böhme, W.: Experimentelle Untersuchungen dynamischer Effekte beim Kerbschlagbiegeversuch, Dissertation TH Darmstadt.
- [8] Hohe, J., Hardenacke, V., Luckow, S., Siegele, D.: An enhanced probabilistic model for cleavage fracture assessment accounting for local constraint effects, Eng. Frac. Mech. 77 (2010) 3573-3591.
- [9] Hohe J, Friedmann V, Wenck J, Siegele D.: Assessment of the role of micro defect nucleation in probabilistic modeling of cleavage fracture. Engng Fract Mech 2008; 75: 3306–27.
- [10] Griffith, A.A.: The phenomena of rupture and flow in solids, Phil. Trans. Roy. Soc. London A221 (1921) 163-198.
- [11] Beremin, F.M.: A local criterion for cleavage fracture of a nuclear pressure vessel steel, Metall. Trans. 14A (1983) 2277-2287.
- [12] Faleskog, J., Kroon, M. and Öberg, H.: A probabilistic model for cleavage fracture with a length scale – parameter estimation and predictions of stationary crack experiments, Eng. Frac. Mech. 71 (2004) 57-79.
- [13] Hardenacke, V.: Verbesserung lokaler Spaltbruchmodelle unter Berücksichtigung mikromechanischer Vorgänge, Dissertation Karlsruher Institut für Technologie (KIT), 2015.
- [14] Böhme, W., Reichert, T. and Mayer, U., 2013. Assessment of dynamic fracture toughness values KJc and reference temperatures $T_{0,X}$ determined for a German RPV steel at elevated loading rates according to ASTM E1921, 22nd Int. Conf. on Structural Mechanics in Reactor Technology, SMiRT-22, San Francisco, USA, August 18-23, 2013.
- [15] Mudry, F.: A local approach to cleavage fracture, Nucl. Eng. Des. 105, 65-76, 1987.